PAPER

Nanoclay-based 3D printed scaffolds promote vascular ingrowth *ex vivo* and generate bone mineral tissue *in vitro* and *in vivo*

Gianluca Cidonio[1,2], Michael Glinka[1] , Yang-Hee Kim[1], Janos M Kanczler[1], Stuart A Lanham[1], Tilman Ahlfeld[3] , Anja Lode[3] , Jonathan I Dawson[1], Michael Gelinsky[3] and Richard O C Oreffo[1,4,5]

1   Bone and Joint Research Group, Centre for Human Development, Stem Cells and Regeneration, Institute of Developmental Sciences, University of Southampton, Southampton, United Kingdom
2   Center for Life Nano Science, Istituto Italiano di Tecnologia, Viale Regina Elena 291, 00161 Rome, Italy
3   Centre for Translational Bone, Joint and Soft Tissue Research, University Hospital Carl Gustav Carus and Faculty of Medicine, Technische Universität Dresden, Dresden, Germany
4   College of Biomedical Engineering, China Medical University, Taichung 40402, Taiwan

E-mail: richard.oreffo@soton.ac.uk

Abstract

Acellular soft hydrogels are not ideal for hard tissue engineering given their poor mechanical stability, however, in combination with cellular components offer significant promise for tissue regeneration. Indeed, nanocomposite bioinks provide an attractive platform to deliver human bone marrow stromal cells (HBMSCs) in three dimensions producing cell-laden constructs that aim to facilitate bone repair and functionality. Here we present the *in vitro, ex vivo* and *in vivo* investigation of bioprinted HBMSCs encapsulated in a nanoclay-based bioink to produce viable and functional three-dimensional constructs. HBMSC-laden constructs remained viable over 21 d *in vitro* and immediately functional when conditioned with osteogenic media. 3D scaffolds seeded with human umbilical vein endothelial cells (HUVECs) and loaded with vascular endothelial growth factor (VEGF) implanted *ex vivo* into a chick chorioallantoic membrane (CAM) model showed integration and vascularisation after 7 d of incubation. In a pre-clinical *in vivo* application of a nanoclay-based bioink to regenerate skeletal tissue, we demonstrated bone morphogenetic protein-2 (BMP-2) absorbed scaffolds produced extensive mineralisation after 4 weeks (p < 0.0001) compared to the drug-free and alginate controls. In addition, HBMSC-laden 3D printed scaffolds were found to significantly (p < 0.0001) support bone tissue formation *in vivo* compared to acellular and cast scaffolds. These studies illustrate the potential of nanoclay-based bioink, to produce viable and functional constructs for clinically relevant skeletal tissue regeneration.

1. Introduction

Skeletal regeneration using innovative tissue engineering approaches has received considerable attention in recent years. Computer-aided cell and biomaterial deposition, namely 3D bioprinting, has shown significant capacity in manufacturing complex and hierarchically organised constructs able to closely mimic bone structure [1]. Thus, bioprinted constructs offer the potential to replace damaged tissue or as an *in vitro* drug screening platform [2].

3D printed implants should ideally: (i) sustain cell viability and promote cell proliferation, (ii) generate functional constructs within a short period of time after printing and, (iii) stimulate the host microenvironment to aid tissue ingrowth and ultimately tissue infiltration and integration. Acellular 3D bioprinting strategies are typically attractive, relying on the intrinsic functional properties of the printed material to attract host cells to aid tissue integration [3]. For instance, a hyper-elastic bone (HB) construct printed with a blend made of poly(lactic-co-glycolic acid), polycaprolactone and hydroxyapatite (PLGA/PCL/HAp) has recently shown promising potential for *in vivo* application [4]. Human bone

5   Author to whom any correspondence should be addressed

marrow stromal cells (HBMSCs) have been found to actively participate in bone repair when encapsulated in functional hydrogel networks [5, 6] indicating the promise of cell-based strategies to closely recapitulate tissue architecture and functions. As bioprinted tissues promote regeneration *in vivo*, the tissue should be amenable to remodelling, facilitating the formation of structures driven by cellular and physiological requirements [7]. Indeed, hydrogel-like biomaterials can actively facilitate this process with the inclusion of a drug delivery system (e.g. plasmid DNA [8]) or living stem/progenitor cells (e.g. HBMSCs [9]). Acellular scaffolds alone appear insufficient/limited in their ability to aid the complete regeneration of functional bone tissue, therefore a new generation of bioinks are needed to: (i) allow the inclusion of HBMSCs within the implantable construct, (ii) enable sustained drug delivery and, (iii) ultimately promote skeletal differentiation [10].

Nanocomposites represent an attractive class of materials that, as hydrogels, are capable to support cell viability and the fabrication of functional three-dimensional implants [11–14]. Among nanocomposite bioinks, nanoclay-based formulations are particularly attractive given their ability, even at low concentrations, to shear while being extruded and regain their shape upon deposition, while shielding encapsulated cells from damage induced by the printing processes [15]. Laponite® (LAP) is a smectite nanoclay suspension that can self-assemble to form reversible, shear thinning gels [16]. LAP is an attractive rheological enhancer and has been extensively studied for the inherent [17] and indirect [18, 19] ability to stimulate the osteogenic differentiation of HBMSCs *in vitro*, but with limited exploration of its *in vivo* potential.

Recently, LAP has been combined with several polymeric materials [20–27] to produce viable bioinks for cell printing applications. In association with polyethylene glycol (PEG) [22] and with the further addition of alginate [26], LAP displayed improved rheological properties, printability and, at higher clay concentrations, elevated recovery after shear. Similar results have been achieved by Dávila *et al* [25] with the extrusion of LAP-alginate hydrogel to produce high shape fidelity constructs utilising an elevated (5 wt%) concentration of LAP nanodiscs. Thus, these different approaches successfully achieved high shape fidelity constructs although, at the cost of high solid concentrations limiting their potential for functional cell delivery. However, the translational potential of nanocomposite-based 3D printed scaffolds remains to be fully evaluated. Zhai *et al* combined LAP with (N-acryloyl glycinamide) (NAGA) [20] and produced functional implants that could stimulate bone formation *in vivo* compared to blank controls. Nevertheless, the effect of clay or NAGA was not further explored and hence it was unclear whether the LAP had a significant effect *in*

vivo. Zhai *et al* [27] have also recently explored the *in vivo* functionality of clay-based 3D printed scaffolds, but the effect of encapsulated growth factors and the inclusion of primary human bone marrow stromal cells on *ex vivo* and *in vivo* pre-clinical models were not investigated.

We have previously developed [15] a LAP-alginate-methylcellulose bioink that can be extruded at a low polymeric content (3 wt% for each component—LAP-alginate-methylcellulose, termed 3-3-3). The 3-3-3 bioink displays shear upon extrusion and shape recovery immediately after deposition, resulting in the ability to generate large and complex three-dimensional structures via 3D extrusion deposition. The inclusion of LAP enhanced mechanical stability of the construct, supported cell proliferation and sustained drug release characteristics *in vitro*.

The aim of the current study is to fabricate 3D bioprinted implantable cell-laden scaffolds to elicit bone formation both *in vitro* and *in vivo* through harnessing LAP physiochemical properties and the ability of LAP to drive osteogenic differentiation. Herein, our studies have characterized the biocompatibility and functional potential of 3-3-3 bioink printed scaffolds combined with HBMSCs and bone morphogenetic protein-2 (BMP-2) and vascular endothelial growth factor (VEGF) to promote osteogenic differentiation *in vitro*, vascularization *ex vivo* and ectopic bone formation *in vivo*.

2. Materials and methods

2.1. Human bone marrow stromal cells and human umbilical vein endothelial cells isolation and culture

Human bone marrow aspirates were collected from haematologically normal patients undergoing routine elective hip replacement surgery. Only tissue samples that would have been discarded were used following informed consent from the patients in accordance with approval from Southampton & South West Hampshire Local Research Ethics Committee (Ref: 194/99/w). HBMSCs were isolated from bone marrow aspirates following our standard protocol [28]. In brief, bone marrow aspirate was resuspended and washed in alpha modified Eagle's medium (α-MEM, Lonza, UK) to remove excessive fat. The resulting cell suspension was then filtered through a 70 μm cell strainer to remove larger bone fragments still present in the suspension. The sample layered on a density gradient separating solution (LymphoPrep™, Axis-Shield, UK) was centrifuged at 800 g for 40 min (18 °C). The bone marrow mononuclear cell (BMMNC) portion was collected from the layer phase between the LymphoPrep™ and the cell culture medium. The collected BMMNCs were then washed with α-MEM supplemented with 10% v/v fetal bovine serum (FBS, Life technologies, Scotland, UK) and 100 U ml^{-1} penicillin and 100 μg ml^{-1}

streptomycin (Sigma-Aldrich, UK). The cell suspension was plated into 175 cm^2 cell culture flasks (Corning, NY, USA) and maintained at 37 °C and 5% CO_2 balanced air for 5 d without changing the media. Cells were then washed with 1× phosphate buffer saline (PBS, Lonza, UK) and cultured for cell expansion.

Human umbilical vein endothelial cells (HUVECs) were isolated as reported in previous protocols [29, 30] from umbilical cords obtained following signed consent from healthy mothers after normal, full-term deliveries from the Princess Anne Hospital, Southampton, under ethical approval from Southampton & South West Hampshire Local Research Ethics Committee (LREC 05/Q1702/102). Endothelial cells were isolated from the inner interstitium following 45 mins infusion of 5 mg ml^{-1} (w/v) Collagenase B solution (Roche Diagnostics UK) at room temperature. Following digestion, the cell suspension was collected and centrifuged at 156 g for 4 mins. Cells were then cultured in endothelial cell culture medium (ECM) prepared from medium 199 supplemented with 1% Pen/Strep (v/v), 10% FBS (v/v), 0.4% (v/v) Endothelial Cell Growth Supplement/Heparin (ECGS/H) (Promocell, Germany). Cells were maintained in culture at 37 °C, 5% CO_2 balanced air, changing media every 3–4 d.

2.2. Laponite®-alginate-methylcellulose material ink

Laponite®-alginate-methylcellulose bioink was produced as previously described [15] at 3% w/v of each component (3-3-3). After sterilisation of LAP (XLG grade, BYK Additives & Instruments, UK), alginate (alginic acid sodium salt from brown algae, 71238, Sigma, UK) and methylcellulose powder (M0512, Sigma, USA, molecular weight ≈ 88 000 Da, 4000 cP) by an autoclave cycle (126 °C, 1.4 bar). LAP powder was added slowly to sterile deionised water (DW) under rapid agitation and stirred for at least 6 h with a magnetic stirrer in a class II sterile hood. Alginate was then added to the stirring DW in a beaker under sterile conditions. The alginate was allowed to dissolve in DW under constant stirring for 3 h to allow complete dissolution. Methylcellulose powder was included and mixed with a sterile spatula. 3-3-3 bioink was stored at 4 °C overnight to allow complete dissolution of the methylcellulose in the LAP-alginate gel. The final hydrogel solution was sterilised by UV irradiation for 30 min. Alginate hydrogel was prepared for casting by solubilisation of sterile alginate powder in DW under class II laminar flow cabinet. Stirring was carried out for 3 h and the final ink was stored at 4 °C overnight.

2.3. HBMSCs printing for *in vitro* viability and functionality

HBMSCs from a single donor were suspended at a density of 1 × 10^6 cells ml^{-1} in serum-free culture medium. Vybrant® DiD (Cell-Labelling Solution,

V22887, Molecular Probes) was then added to the cell suspension to label viable cells prior to encapsulation. A 5 μl solution of DiD was supplied for each ml of cell suspension and mixed by pipetting. Cell suspension supplemented with DiD was incubated for 20 min at 37 °C. The supernatant was removed following centrifugation and the stained cell pellet resuspended in pre-warmed (37 °C) serum-free culture media. As previously described [15], cells were encapsulated at 1 × 10^6 cell g^{-1} in 3-3-3 bioink and printed. Printing was carried out using the in-house built bioprinter [31] and 410 μm nozzle (Fisnar Europe, UK) to fabricate 4 layers of 10 × 10 mm^2 scaffold with an alternating layer pattern (ABAB, 0°/90°), a layer height of 300 μm and a strand distance of 2 mm. After printing, the scaffolds were incubated for 10 min in sterile 100 mM $CaCl_2$ solution to enable crosslinking. Scaffolds for viability (total n = 12) and functionality (total n = 16) investigations were printed with n = 3 scaffolds used at each time point.

2.4. Viability and proliferation in cell-laden scaffolds

Viability was quantified from confocal images taken after 1, 7, 14 and 21 d of culture *in vitro* following previously employed protocol [15]. Samples were first collected and washed twice with Hank's Balanced Salt Solution (HBSS, Gibco). Calcein AM (C3099, Invitrogen, Thermo Fisher Scientific) was diluted in serum-free culture media following the manufacturer's protocol and added to each cell-laden scaffold. The scaffolds were then incubated at 37 °C and 5% CO_2 balanced air for 1 h. A repeat wash with HBSS was then carried out. Samples were imaged using a confocal scanning microscope (Leica TCS SP5, Leica Microsystems, Wetzlar, Germany). Quantification with ImageJ (1.44p, National Institutes of Health, Bethesda, Maryland, USA) of living cells was performed by comparing, the number of Calcein stained cells and DiD stained cells in the Z-stacks of 15 ROI per time point (n = 3).

Cell density within the scaffolds at different time points was calculated by further analysis of the confocal pictures. A calculation by normalisation of the number of living cells and the volume of interests was carried out. The resulting value was converted into percentage and plotted with reference to the value corresponding to day 1 (set as 100 %).

2.5. HBMSC-laden scaffolds functionality *in vitro*

Alkaline phosphatase (ALP) staining was performed at 1, 7 and 21 d on samples cultured *in vitro* and conditioned with basal or osteogenic media. Basal media was considered as α-MEM supplemented with 10% (v/v) FBS and 100 U ml^{-1} penicillin and 100 μg ml^{-1} streptomycin. Osteogenic cell culture media was prepared from α-MEM supplemented with 10% (v/v) FBS, 1% (v/v) Pen/Strep, 100 μM ascorbate-2-phosphate (AA2P,

Sigma-Aldrich), 10 nM dexamethasone (Dex, Sigma-Aldrich) and 10 nM vitamin D (1α,25-OH$_2$-Vit D3, Sigma-Aldrich). Media was removed and samples washed twice with HBSS. Samples were fixed in 95% ethanol for 10 min. The ethanol solution was removed and samples washed twice with HBSS. The cell-laden and cell monolayer cultures were left to dry for 10 min. ALP staining solution was prepared by the inclusion of 400 μl Naphtol (AS-MX Phosphate Alkaline Solution, 85-5, Sigma-Aldrich, UK) and 0.0024 g of Fast Violet Salt (F1631 Sigma-Aldrich, UK) in 9.6 ml of DW. The solution was then pipetted onto samples, which were incubated at 37 °C for 1 h. The reaction was then stopped by HBSS. Samples were stored at 4 °C overnight and imaged with Zeiss Axiovert 200 (Carl Zeiss, Germany) the following day.

2.6. Chick chorioallantoic membrane (CAM) assay

2.6.1. Sample fabrication
Scaffolds were printed using sterile 3-3-3 bioink. For an initial CAM study, scaffolds of different dimensions, with 8, 10 and 12 mm side length, were fabricated (n = 6 for each treatment group), stored in HBSS at 4 °C overnight and implanted the following day. Control group was prepared by casting 3-3-3. For a second CAM study, acellular scaffolds were produced with a 10 × 10 mm lattice base area and a strand distance of 2.5 mm and divided into four groups: (i) 3D printed (n = 6), (ii) 3D printed loaded with VEGF (n = 6), (iii) 3D printed seeded with HUVECs (n = 6) and (iv) 3D printed loaded with VEGF and seeded with HUVECs (n = 6). After printing and crosslinking, scaffolds were allowed to reach swelling stability in full cell culture media for 3 h at 37 °C and 5% CO$_2$. HUVECs were seeded at a density of 6×10^5 cell per scaffold (group iii and iv, n = 12). Cells in 500 μl were deposited onto scaffolds and incubate at 37 °C and 5% CO$_2$ to allow attachment for 3 h. Cell culture media was then inserted to submerge the scaffolds and left overnight at 37 °C and 5% CO$_2$. Recombinant human VEGF 165 (Peprotech, USA) was diluted to 100 μg ml^{-1} in HBSS solution and pipetted onto the printed scaffolds (group ii and iv, n = 12). VEGF was absorbed onto printed scaffolds for 60 min maintaining well plates in close contact with ice. HBSS was used to wash out unbound VEGF before implantation.

2.6.2. Implantation, extraction and Chalkley score
All animal procedures were carried out in accordance with the guidelines and regulations laid down in the Animals (Scientific Procedures) Act 1986. Chick embryo CAM model was carried out according to Home Office Approval, UK (Project license—PPL P3E01C456). Chicken eggs were purchased from Medeggs (Norfolk, UK), received and incubated in a Hatchmaster incubator (Brinsea, UK) for 7 d at 37 °C in a 60% humidified atmosphere and 1 h rotation. DW was supplemented every two days to ensure the

maintenance of a humidified environment in the egg incubator. After 7 d, eggs were prepared for implantation. Eggs were candled to assess embryo development and the presence of a vascularised membrane. An empty 1 cm^2 window was created to allow scaffold implantation. After the scaffolds were implanted the window was immediately sealed with a thin film of transparent sterile Parafilm (Bemis™, Parafilm M™, Laboratory Wrapping Film, Fisher Scientific, UK). Eggs were then incubated in a Hatchmaster incubator for 7 d at 37 °C in a 60% humidified atmosphere without any rotation.

The infiltration of blood vessels throughout the implanted scaffolds was evaluated and quantified by Chalkley scoring as previously described [32]. Briefly, integrated samples were collected and observed under a stereo light microscope through a Chalkley eyepiece graticule placed in one of the microscope ocular, projected on the scaffold that was being examined and the number of vessels was obtained and registered from five independent counts. The scores were registered for each integrated sample.

2.7. *In vivo* assessment of subcutaneous bone formation

All procedures were performed with prior received ethical approval (P96B16FBD) and carried out in accordance with the regulations as laid down in the Animals (Scientific Procedures) Act 1986 and in accordance with institutional guidelines. Animals had ad libitum access to standard mouse chow and water.

2.8. Subcutaneous implantation *in vivo* of BMP-2 loaded 3D printed scaffolds

2.8.1. Preparation of casted alginate and 3D printed 3-3-3 scaffolds for BMP-2 delivery in vivo
Casted alginate gel (3% w/v) scaffolds were fabricated as negative (BMP-2 free) and positive (loaded with BMP-2) controls for functional mineral formation *in vivo*. Alginate scaffolds were crosslinked with 100 mM of CaCl$_2$ for 10 min. Crosslinking solution was then removed, and scaffolds were washed (×5) with HBSS. Scaffolds were then blotted dry and weighed to confirm their weight was consistent with 3D printed scaffolds. Alginate casted scaffolds weighed 0.164 ± 0.02 g. Scaffolds were kept dry at 4 °C overnight in a solution-free well plate for BMP-2 loading and scaffold implantation the following day. 3D printed scaffolds were fabricated using 3-3-3 as material ink. A sterile 410 μm cylindrical blunt nozzle was used. 3D scaffolds (n = 12) were printed sequentially and crosslinked with 100 mM of CaCl$_2$ for 10 min after printing. Crosslinking solution was then removed, and scaffolds were washed (x5) with HBSS. The weight of the printed scaffolds was recorded as 0.165 ± 0.03 g. Scaffolds were stored dry at 4 °C overnight in a 6-well plate for BMP-2 loading and scaffold implantation the following day.

2.8.2. BMP-2 loading and implantation of scaffolds in MF-1 mice

MF-1 wild type (WT) mice were bred in-house. *In vivo* experimental design consisted of the implantation, subcutaneously of n = 3 scaffolds of 4 treatment group and a single sham control in a total of n = 4 MF-1 WT mice. Treatment groups were: (i) alginate, (ii) alginate absorbed with BMP-2, (iii) 3D printed 3-3-3 and (iv) 3D printed 3-3-3 absorbed with BMP-2. A BMP-2 solution was diluted to a final concentration of 10 μg ml^{-1}. The solution was then left to absorb on alginate casted and 3D printed 3-3-3 scaffolds for 1 h prior to implantation. Scaffolds were maintained on ice during the loading of BMP-2 to avoid BMP-2 degradation. Scaffolds were blotted dry after a wash with HBSS. Mice were first weighed and then anaesthetised with fentanyl–fluanisone (Hypnorm, Janssen-Cilag Ltd) and midazolam (Hypnovel, Roche Ltd) in sterile water at a ratio of 1:1 and a dose of 10 ml kg^{-1} intraperitoneally. A total of three midline dorsal incisions per side were made after shaving and an ethanol disinfection of the outer skin. A total of n = 3 printed scaffolds with BMP-2 and n = 3 printed scaffolds BMP-2 free were implanted on each side. Immediately following surgery, mice were housed in a temperature-controlled cage (with optimal temperature of 28 °C) until the complete restoration of motor functions. Mice were housed in cages for up to 4 weeks.

2.9. Subcutaneous implantation *in vivo* of HBMSC-laden 3D bioprinted scaffolds

2.9.1. Preparation of casted and 3D printed 3-3-3 constructs for HBMSC-encapsulation for in vivo implantation

Casted hydrogels were fabricated as control for functional bone formation *in vivo* and divided into two groups: (i) acellular or (ii) HBMSC-laden scaffolds with 1 × 10^6 cells ml^{-1}. Casted scaffolds were crosslinked in 100 mM CaCl$_2$ for 10 min and subsequently washed (×5) with HBSS. Casted scaffolds (n = 3) were blotted dry and weighed to confirm similar mass to the 3D printed scaffolds. The acellular and cell-laden casted scaffolds weighed 0.163 ± 0.74 g and 0.162 ± 0.81 g respectively. A total of n = 12 samples for each treatment group (acellular and cell-laden) were produced. Only n = 9 samples per group were used for the implantation. The remaining scaffolds (n = 3) were maintained in culture *in vitro* for further comparison after 8 weeks. Scaffolds were incubated at 37 °C and 5% CO$_2$ overnight and implanted the following day.

3D printed acellular and cell-laden 3-3-3 scaffolds were fabricated sequentially and crosslinked for 10 min with 100 mM CaCl$_2$ then washed (x5) with HBSS. The weight of 3D printed scaffolds, (n = 3) were 0.162 ± 0.04 g and 0.163 ± 0.34 g for acellular and cell-laden scaffolds respectively. Samples (n = 12) were produced for acellular and cell-laden printed 3-3-3 scaffolds. Samples for implantation (n = 9) were cultured at 37 °C and 5% CO$_2$ balanced air overnight and implanted the following day. The remaining samples (n = 3) were kept in culture *in vitro* for further comparison after 8 weeks.

2.9.2. Implantation of scaffolds in BALB/c athymic nude mice

The study consisted of the implantation of n = 9 scaffolds of four treatment groups in n = 9 BALB c^{-1} athymic nude mice. Male athymic immunodeficient mice were purchased from Envigo, UK and acclimatised for a minimum of 1 week prior to experimentation. Treatment groups, all realised using the 3-3-3 bioink, were: (i) casted, (ii) casted with encapsulated cells, (iii) 3D printed and (iv) 3D printed with encapsulated cells. Scaffolds were washed with serum-free media and maintained in the same media during surgery. Scaffolds were then blotted dry after a single wash with HBSS. Animals were anaesthetised as described previously. A total of n = 8 printed scaffolds for each treatment group were implanted, two for each side, in a randomised distribution. Incisions were closed using sterile metal michel clips. Scaffolds were implanted sequentially. An overall number of n = 32 scaffolds were implanted in the subcutaneous pocket of n = 9 mice. Finally, one scaffold from each treatment group were implanted in a single mouse to be monitored, from the day of implantation (0 weeks) until 8 weeks, using micro-CT imaging. Sutures instead of metal clips were applied to avoid interference with CT readings. After each surgical intervention, mice were housed temporally in a temperature-controlled ventilated cages with a desired temperature maintained at 28 °C. After full recovery from surgery, animals were housed in ventilated cages and monitored continuously up until 8 weeks.

2.10. Micro-computed tomography images

A micro-computed tomography (micro-CT) scanner (Bruker Skyscan 1176) was used to collect all the CT images of scaffolds implanted from the two subcutaneous mouse experiments. Mice were scanned at 4 weeks for the subcutaneous implantation in MF-1 mice and at 4, 6, and 8 weeks for the implantation studies performed in BALB/c nude mice. Animals were anaesthetised with Isoflurane (IsoFlo® Zoetis, UK). Scans were all carried out with a pixel size of 35 μm, 65 kV, 385 μA, 0.7° rotation step, 135 ms exposure, and an aluminium filter (Al) of 1 mm.

CT representative reconstructions were obtained using NRecon (Bruker). Quantitative analysis for new bone formation was carried out using CTAn software v.1.17.7.2 (Bruker) to assess bone volume (BV) and average bone mineral density. Two bone phantoms (0.25 g cm^{-3} and 0.75 g cm^{-3} bone density) were used as reference, and were scanned with the same parameters as implanted samples. After the final CT

scans, anesthetised mice were sacrificed and samples extracted. A midline incision was made on the spine and macroscopic images of integrated scaffolds were taken.

2.11. Histological analysis
Samples implanted both *ex vivo* or *in vivo* were fixed in 4% paraformaldehyde (PFA) solution overnight at 4 °C. Optimal cutting temperature (OCT, Thermo Fisher Scientific) medium was then used after 12 h. Samples were stored at −80 °C overnight, and sectioning performed the following day. A Cryostat (CM 1850, Leica Biosystems, Germany) was used to produce tissue sections of 8 μm. Kawamoto's film method [33] was used to collect the sections and Goldner's Trichrome and Von Kossa staining subsequently carried out on cryotape. After staining, Super Cryomounting Medium (SCMM) type R3 (Section LAB, Co. Ltd. Japan) was used for mounting. UV light curing was carried out for 30 min to allow photopolymerisation of the SCMM. Slides were stored at room temperature and imaged the following day with a Zeiss Axiovert 200 (Carl Zeiss, Germany). Samples extracted after *in vivo* implantation were processed, sectioned and stained with Alcian Blue and Sirius Red following standard protocol previously employed [34].

2.12. Statistical analysis
The statistical analyses were performed using Graph-Pad Prism software 7 (Graph Pad Software Inc. La Jolla, CA). Variation in the data were assessed by D'Agostino-Pearson normality test. Differences among groups were determined by one-way and two-way ANOVA with a post Tukey's test according to experimental design and considered to be significantly different if P < 0.05.

3. Results

3.1. Printing of HBMSCs in a nanocomposite ink preserves cell viability and supports osteogenic differentiation *in vitro*
To evaluate viability, proliferation and functionality, HBMSCs were encapsulated in the 3-3-3 bioink scaffold. Constructs were maintained in culture and imaged at 1 (figure 1(a)-i), 7 (figure 1(a)-ii), 14 (figure 1(a)-iii) and 21 (figure 1(a)-iv) days. Cells were observed to display and retain a rounded morphology for up to 21 d with negligible cell spreading in three-dimensions. HBMSCs viability (figure 1(b)-i) was quantified following image analysis with viability preserved at 90% from day 7 onwards. After 7 d of culture, the density of the printed HBMSCs (figure 1(b)-ii) was found to be significantly higher (p < 0.0001) than at day 1, decreasing after 7 d (p < 0.0001) and subsequently plateauing over 21 d in culture.

The functionality of HBMSC-laden 3D printed scaffolds was investigated using ALP and Von Kossa staining after 1, 7 and 21 d of culture *in vitro*. To confirm the absence of mineral deposition in acellular 3-3-3 scaffolds, Von Kossa was carried out prior and after crosslinking confirming negative staining (stacks.iop.org/BF/12/035010/mmedia supporting figure 1) compared to positive control. Von Kossa staining indicated mineralisation of the printed 3-3-3 cellular constructs. 3D printed cell-laden scaffolds cultured in basal and osteogenic media displayed decreased ALP expression (figure 1(c)-i,iii) together with increased calcium mineral deposition (figure 1(c)-ii,iv) over 21 d. Overall, culture in basal conditions produced reduced ALP and mineral staining compared to 3-3-3 constructs maintained in osteogenic conditions.

3.2. 3D printed nanocomposite scaffolds elicit a response in vascular remodelling in an *ex vivo* chorioallantoic (CAM) model
Acellular 3D printed scaffolds of various sizes were implanted in the vascularised CAM of 7-day-old developing chick embryos to assess vessel penetration and stability *ex vivo* (figure 2(a)). Control casted scaffolds (figure 2(a)-i) revealed negligible capillary penetration throughout the structure. 3D printed scaffolds with surface area of 8 × 8 mm (figure 2(a)-ii), 10 × 10 mm (figure 2(a)-iii), 12 × 12 mm (figure 2(a)-iv) displayed excellent integration, with blood vessel penetration throughout the large pores. Chalkley score analysis (figure 2(b)) revealed a significant difference (p < 0.001) between the 10 × 10 mm group constructs compared to the empty and control groups. The remaining scaffold constructs (8 × 8 mm and 12 × 12 mm) showed reduced integration, although significantly higher vascular infiltration compared to empty and control groups (p < 0.01).

To investigate the functional effect of the angiogenic stimulant (VEGF) and endothelial cells (HUVECs) on 3D printed scaffolds, constructs were implanted into a CAM model (figure 2(c)). 3D printed control (figure 2(c)-i) scaffolds were found integrated with some pores containing blood vessels, but with large portions lacking capillary penetration. VEGF-loaded scaffolds (figure 2(c)-ii) and HUVECs-seeded samples (figure 2(c)-iii) were found to be infiltrated with vessels penetrating through the printed structure confirming scaffold integration and blood vessel penetration. Major pores displayed an irregular shape as a consequence of remodelling and *in vivo* degradation, filled with major blood vessels. 3D printed scaffolds loaded with VEGF and seeded with HUVECs (figure 2(c)-iv) were extensively integrated with the CAM membrane with vessels penetrating the pores of the printed structure and with major capillaries surrounding the scaffolds indicating the vascularisation of the inner, as well as the outer, portion of the printed construct. Chalkley score analysis (figure 2(d)) showed scaffolds with VEGF
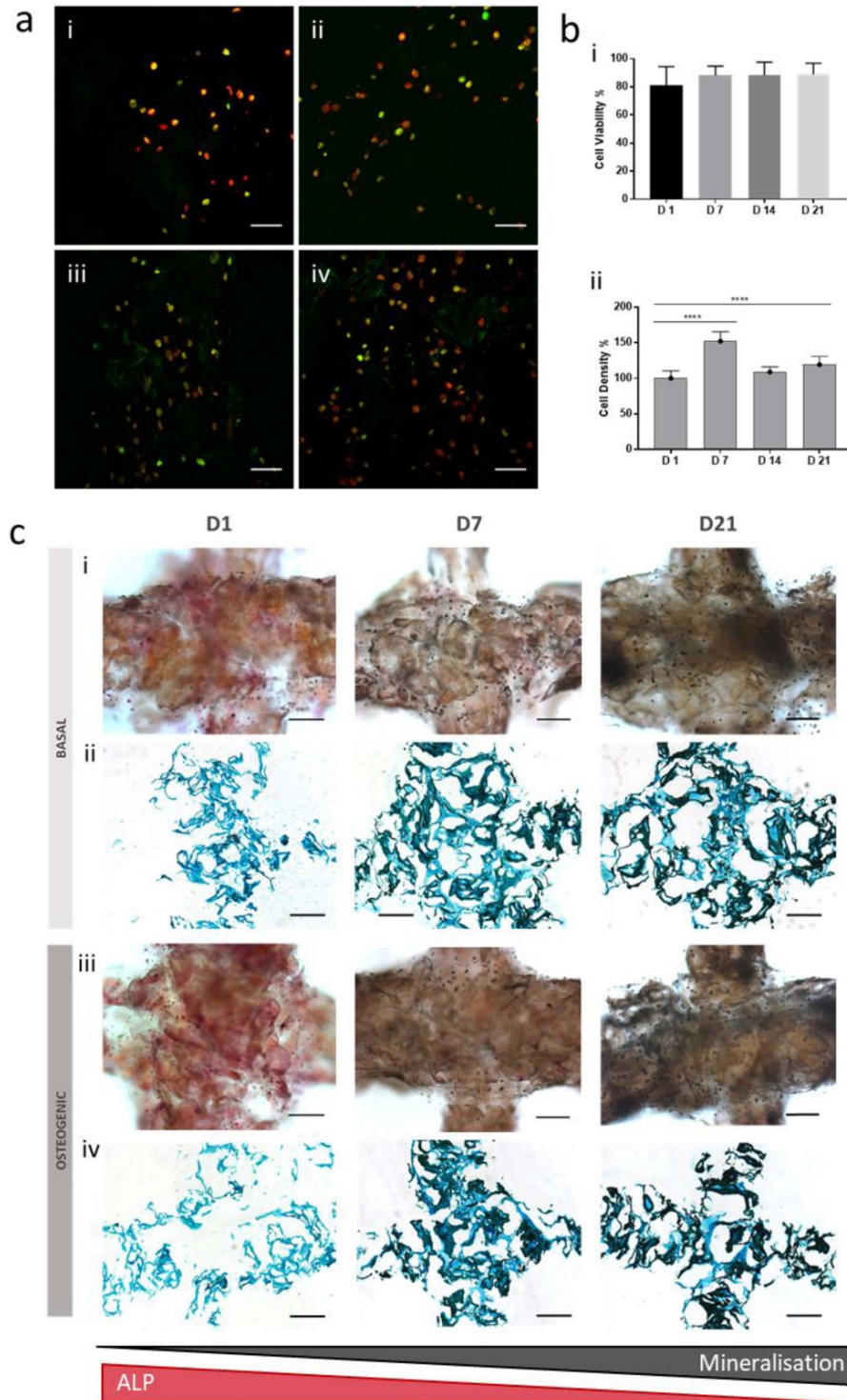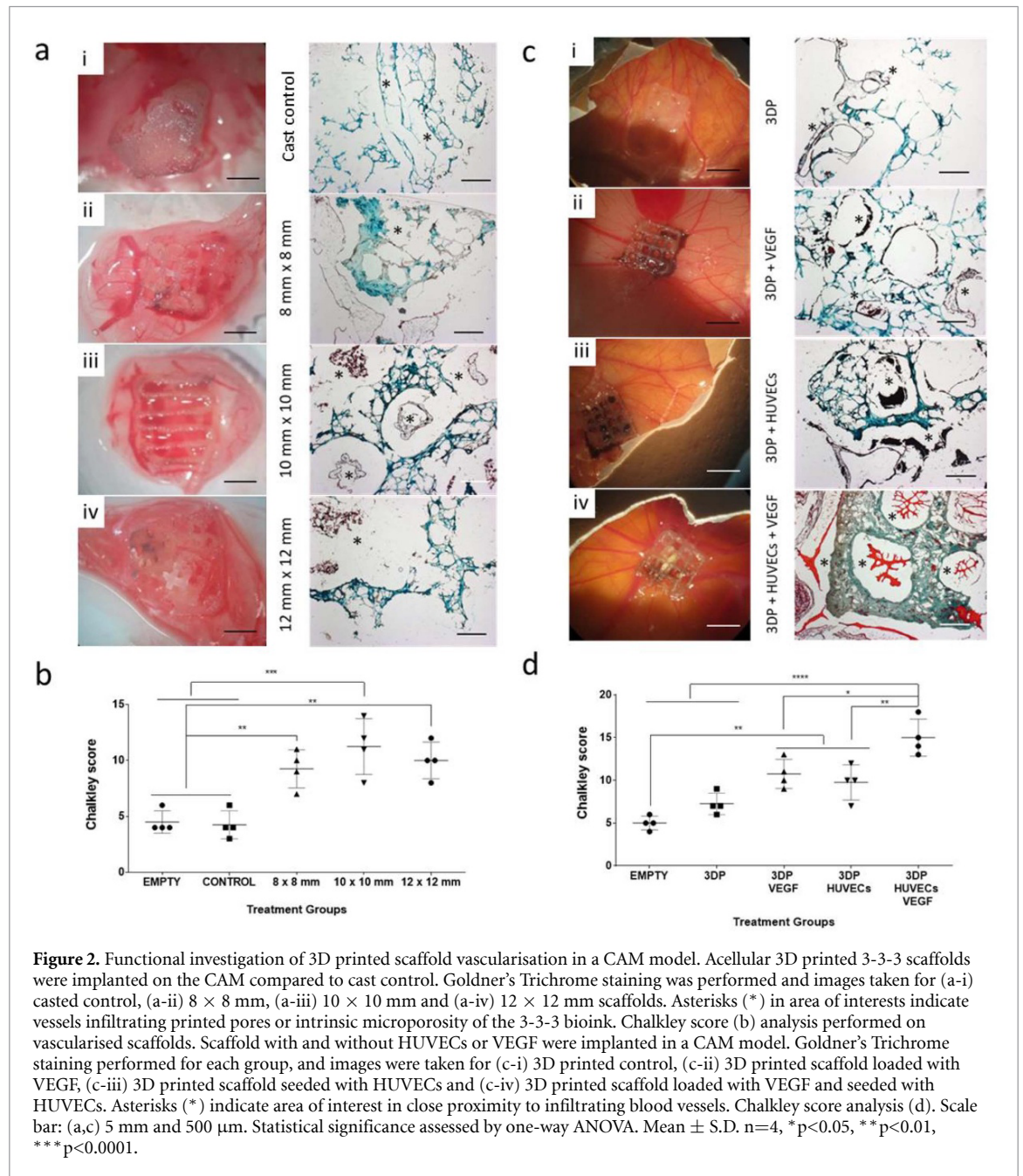
Figure 1. HBMSC-laden 3D printed scaffolds *in vitro* viability and functionality. Confocal microscopic images of HBMSCs-laden scaffolds at (a-i) 1, (a-ii) 7, (a-iii) 14 and (a-iv) 21 days of *in vitro* incubation. Cells were stained with DiD labelling solution (red) while mitotically active cells were stained with Calcein AM (green). Cell viability (b-i) and (b-ii) density quantification. Cell viability percentages were obtained from the calculated difference between viable and total cells. Dead cells comprised the fraction not stained with Calcein AM. Functional evaluation of scaffolds cultured in basal and osteogenic media via ALP (c-i, c-iii) and Von Kossa (c-ii, c-iv) staining respectively. Scale bar: (a) 100 μm, (c) 250 μm. Statistical significances were assessed by one-way ANOVA. Mean ± S.D. n=3, ****p<0.0001.

and HUVECs alone displayed higher infiltration of blood vessels (p < 0.01) than samples lacking any scaffold (empty). 3D printed scaffolds loaded with VEGF and seeded with HUVECs showed a significant (p < 0.0001) difference in vascular penetration compared to empty and control 3D printed scaffolds. The combination of VEGF and HUVECs with printed scaffolds produced a significantly enhanced effect compared to HUVECs seeded alone (p < 0.01) and VEGF loaded alone (p < 0.05).

Figure 2. Functional investigation of 3D printed scaffold vascularisation in a CAM model. Acellular 3D printed 3-3-3 scaffolds were implanted on the CAM compared to cast control. Goldner's Trichrome staining was performed and images taken for (a-i) casted control, (a-ii) 8 × 8 mm, (a-iii) 10 × 10 mm and (a-iv) 12 × 12 mm scaffolds. Asterisks (*) in area of interests indicate vessels infiltrating printed pores or intrinsic microporosity of the 3-3-3 bioink. Chalkley score (b) analysis performed on vascularised scaffolds. Scaffold with and without HUVECs or VEGF were implanted in a CAM model. Goldner's Trichrome staining performed for each group, and images were taken for (c-i) 3D printed control, (c-ii) 3D printed scaffold loaded with VEGF, (c-iii) 3D printed scaffold seeded with HUVECs and (c-iv) 3D printed scaffold loaded with VEGF and seeded with HUVECs. Asterisks (*) indicate area of interest in close proximity to infiltrating blood vessels. Chalkley score analysis (d). Scale bar: (a,c) 5 mm and 500 μm. Statistical significance assessed by one-way ANOVA. Mean ± S.D. n=4, *p<0.05, **p<0.01, ***p<0.0001.
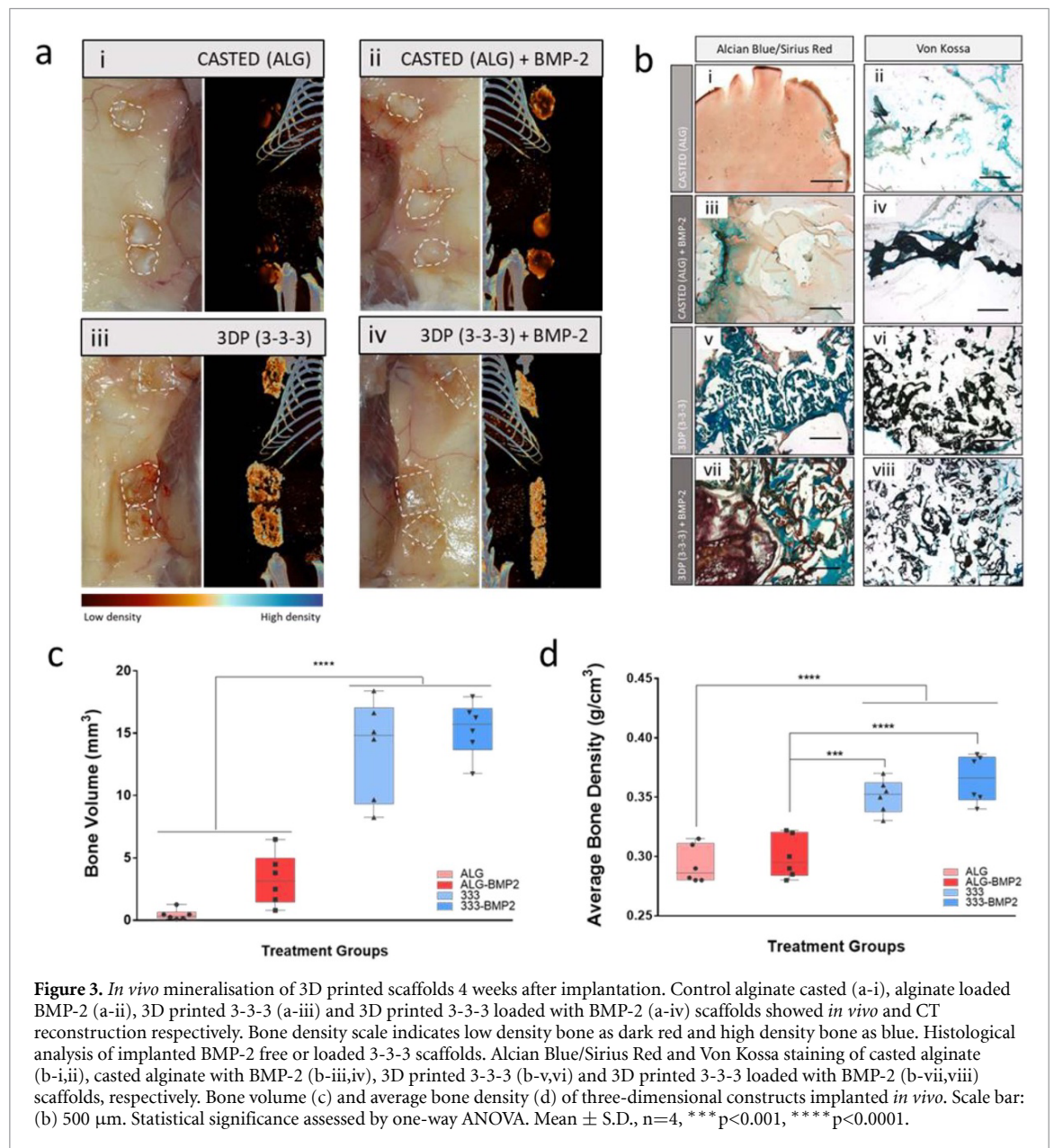
3.3. *In vivo* BMP-2-loaded nanosilicate-based scaffolds produce new bone in a murine subcutaneous implant model

To test the *in vivo* functionality of the 3-3-3 bioink, 3D scaffolds were fabricated and implanted subcutaneously into MF-1 mice. BMP-2 was loaded within the scaffolds to investigate the capacity of the 3-3-3 bioink for retention and localisation of growth factors of interest for skeletal regeneration (figure 3). Control acellular 3-3-3 scaffolds were CT scanned to confirm the absence of any mineral deposition before implantation using bone phantoms as controls (supporting figure 2) with the nanosilicate based scaffolds observed to have no density above $0.1 \, \text{g cm}^{-3}$. The BMP-2-free casted alginate retained their spherical appearance and CT images confirmed

limited mineral deposition (figure 3(a)-i, supporting figure 3(a)). BMP-2 loaded casted alginate samples displayed greater mineralisation after only 4 weeks (figure 3(a)-ii, supporting figure 3(b)). BMP-2 free (figure 3(a)-iii, supporting figure 3(c)) and loaded (figure 3(a)-iv, supporting figure 3(d)) 3-3-3 scaffolds were found to be partially degraded although the scaffolds retained their lattice structure and extensive mineralisation could be observed compared to negative and positive controls.

Histological analysis of BMP-2-free casted alginate scaffolds revealed the presence of limited GAGs in the sample area surrounded by a discrete layer of collagen (figure 3(b)-i) and an absence of calcified tissue (figure 3(b)-ii). BMP-2-loaded casted alginate scaffolds (figure 3(b)-iii) stained positively for GAGs

Figure 3. *In vivo* mineralisation of 3D printed scaffolds 4 weeks after implantation. Control alginate casted (a-i), alginate loaded BMP-2 (a-ii), 3D printed 3-3-3 (a-iii) and 3D printed 3-3-3 loaded with BMP-2 (a-iv) scaffolds showed *in vivo* and CT reconstruction respectively. Bone density scale indicates low density bone as dark red and high density bone as blue. Histological analysis of implanted BMP-2 free or loaded 3-3-3 scaffolds. Alcian Blue/Sirius Red and Von Kossa staining of casted alginate (b-i,ii), casted alginate with BMP-2 (b-iii,iv), 3D printed 3-3-3 (b-v,vi) and 3D printed 3-3-3 loaded with BMP-2 (b-vii,viii) scaffolds, respectively. Bone volume (c) and average bone density (d) of three-dimensional constructs implanted *in vivo*. Scale bar: (b) 500 μm. Statistical significance assessed by one-way ANOVA. Mean ± S.D., n=4, ***p<0.001, ****p<0.0001.

content and mineralised content (figure 3(b)-iv) although expression was limited throughout the constructs. GAGs penetration in drug-free 3D printed scaffolds (figure 3(b)-v) was enhanced compared to cast and BMP-2-casted controls with mineral deposition (figure 3(b)-vi) localised near the scaffold-tissue interface (figure 3(b)-vi). BMP-2 loaded onto the 3D printed scaffold (figure 3(b)-vii) displayed collagenous tissue penetrating the printed constructs and extensive mineralisation (figure 3(b)-viii) across the entire scaffold.

Bone volume (figure 3(c)) and average bone density (figure 3(d)) were quantified across all implanted scaffolds. 3D printed scaffolds loaded with BMP-2 and drug-free showed significantly higher bone volume ($p < 0.0001$) than BMP-2 loaded and free alginate controls respectively. Average bone density analysis revealed BMP-2 loaded 3D printed scaffolds generated significantly higher bone density

than drug-loaded and free casted control scaffolds ($p < 0.0001$). Surprisingly, the 3D printed drug-free scaffolds showed significantly higher average bone density in comparison to BMP-2-loaded alginate casted control ($p < 0.001$) and casted drug-free scaffolds ($p < 0.0001$).

3.4. *In vivo* implantation of HBMSC-laden nanocomposite scaffolds generate significant new bone in a subcutaneous implant model

To evaluate the potential of HBMSC-laden 3D printed scaffolds to generate *de novo* bone tissue *in vivo*, acellular and cell-laden lattice and casted scaffolds were fabricated and implanted in athymic BALB/c mice. To investigate bone formation in a unique host, one sample of each treatment group was implanted. Casted (cranial posterior evaluation) and HBMSC-laden casted (caudal posterior evaluation) images were taken at each time point (supporting figure

4(a)). After 2 weeks, HBMSC-laden scaffolds showed the initial formation of mineral depositions, while the casted scaffold displayed no mineral deposition even after 4 weeks. Following 6 weeks of implantation, casted acellular scaffolds displayed mineralised tissue, as did the HBMSC-laden casted scaffolds. At 8 weeks, the scaffolds displayed extensive mineralisation which had started to remodel in comparison to 6-weeks samples. Implanted 3D printed (cranial posterior) and HBMSC-laden 3D printed (caudal posterior) scaffolds were imaged at each time point (supporting figure 4(b)). Acellular and cell-laden 3D printed scaffolds displayed detectable mineralisation after only 2 weeks. 3D printed scaffolds differed from the casted controls with cluster-like mineralisation observed. At 4 weeks post-implantation, acellular and HBMSC-laden scaffolds displayed extensive mineralisation, with the mineral content observed to accrue over 8 weeks. Acellular printed scaffolds displayed rapid mineralisation with a significant increase between 4 and 6 weeks. 3D printed HBMSCs encapsulated scaffolds increased in mineral density over 8 weeks, with only modest changes between weeks 6 and 8.

To assess bone formation in a randomised *in vivo* study, treatment groups were implanted in pairs subcutaneously. Casted acellular 3-3-3 scaffolds (figure 4(a)-i) were observed to be mineralised on the outer surface after 8 weeks post implantation. Full-field view of the scaffolds revealed mineral deposition across the entire outer surface with discrete high mineral density regions. Inner CT scan of casted sample revealed a non-mineralised core. HBMSC-laden casted 3-3-3 (figure 4(a)-ii) showed mineral deposition on the outer surface with reduced mineralisation at the core. Acellular 3D printed 3-3-3 scaffolds (figure 4(a)-iii) displayed rapid mineral deposition over 8 weeks, with increased mineral density. Mineral deposition appeared expressed in a cluster-like fashion and was also observed within the inner core of the printed scaffold. HBMSC-laden 3D printed 3-3-3 scaffolds (figure 4(a)-iv) showed extensive mineralisation that was also observed within the core of the constructs.

Bone volume (figure 4(b)) did not vary significantly between treatment groups after 2 weeks of implantation. At 4 weeks, 3D printed scaffolds loaded with HBMSCs showed significant differences in bone volume with acellular casted, 3D printed ($p < 0.001$) and HBMSC-laden casted ($p < 0.0001$) constructs. After 6 weeks, cell-laden 3D printed resulted in significant ($p < 0.0001$) bone formation compared to acellular and cellular casted controls and HBMSC-free printed scaffolds. Following 8 weeks of implantation, HBMSC-laden printed scaffolds showed significant ($p < 0.0001$) differences in bone volume formation in comparison to acellular casted and printed as well as HBMSC-laden casted scaffolds.

Data reported in supporting figure 5(a) illustrates the changes in bone volume from 2 weeks through to 8 weeks of implantation. Acellular casted scaffolds showed a significant increase in bone volume at 6 ($p < 0.01$) and 8 ($p < 0.0001$) weeks respectively compared to the 2 weeks scan. HBMSC-laden casted scaffolds showed a significant increase in bone volume at 8 weeks ($p < 0.01$) compared to the initial scan at 2 weeks. Acellular 3D printed scaffolds displayed significantly augmented bone volume at 8 weeks compared to 2 ($p < 0.0001$) and 4 ($p < 0.01$) weeks scan sets. A significant increase ($p < 0.01$) was observed after 6 weeks of implantation. HBMSC-laden printed scaffolds showed a significant increase in bone volume ($p < 0.0001$) at all the time points examined.

Average bone density (figure 4(c)) analysis indicated no significant differences between treatment groups at 2, 4, 6 and 8 weeks after implantation (supporting figure 5(b) demonstrates the quantitative changes in bone density each week for each treatment group). Acellular casted scaffolds showed a linear increase in bone density with a significant increase in density from 2 to 8 weeks ($p < 0.01$). HBMSC-laden casted scaffolds showed a significant increase in bone density after 6 ($p < 0.01$) and 8 ($p < 0.001$) weeks. Acellular and HBMSCs-laden 3D printed scaffolds displayed an overall significant change in density between 2 and 8 weeks ($p < 0.001$).

Casted scaffolds stained for Alcian blue/Sirius red (figure 4(d)-i) displayed diffused GAGs and collagen distribution over the entire scaffold. Mouse cells were found to penetrate the drug-free casted scaffolds with mineral deposition localised in a limited portion of the scaffold (figure 4(d)-ii). Casted control scaffolds loaded with HBMSCs (figure 4(d)-iii) displayed a paucity of GAGs comparable to the acellular control. Extensive collagen staining was found distributed throughout the entire scaffold, in correspondence of encapsulated cells. Von Kossa staining (figure 4(d)-iv) showed diffused large mineralised tissue in the scaffold. Acellular 3D printed samples (figure 4(d)-v), similar to acellular casted scaffolds were found positively stained for GAGs and murine cells were found to have penetrated the structure. Mineral deposition (figure 4(d)-vi) was found to be significantly impaired and only scattered localised deposition of mineral was observed throughout the scaffold after implantation. HBMSC-laden 3D printed implants (figure 4(d)-vii) displayed high levels of collagenous tissue throughout with extensive presence of printed cells in close proximity resulting in a compact tissue-like structure. Integration with surrounding tissue was observed extensively with collagenous tissue throughout the core of the scaffold. Cell-laden scaffolds were found to be mineralised in cluster-like deposited nodules (figure 4(d)-viii) that were found preferentially located on the outer surface of the scaffold.
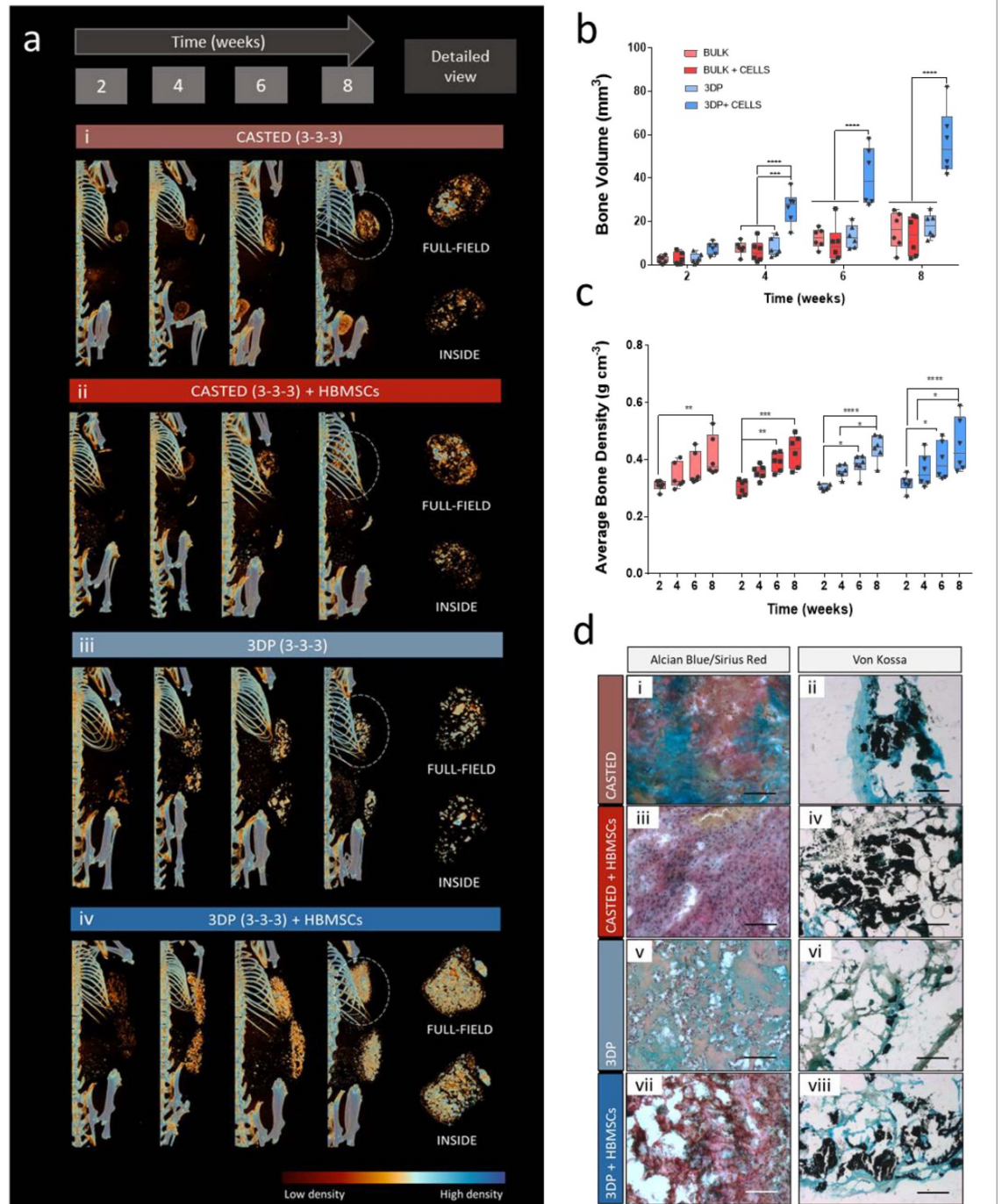
Figure 4. *In vivo* bone formation of 3D cell-laden nanocomposite scaffolds. Posterior CT images of acellular casted (a-i), HBMSC-laden casted (a-ii), acellular 3D printed (a-iii) and HBMSC-laden 3D printed (a-iv) scaffolds at 2, 4, 6 and 8 weeks. Full-field top and inside view of selected scaffolds. Bone density scale indicates low-density bone as dark red and high-density bone as blue. Bone volume (b) and average bone density (c) of three-dimensional constructs implanted *in vivo* were analysed by treatment conditions, including casted, casted with HBMSCs, 3D printed, and 3D printed with HBMSCs. Histological analysis of implanted acellular and cell-laden 3-3-3 scaffolds. Casted (d-i,ii), HBMSC-laden casted (d-iii,iv), 3D printed (d-v,vi) and HBMSC-laden 3D printed (d-vii,viii) scaffolds stained respectively with Alcian blue/Sirius red and Von Kossa staining. Scale bar: (d) 100 μm. Statistical significance assessed by two-way ANOVA. Mean ± S.D., n=6, *p<0.05, **p<0.01, ***p<0.001, ****p<0.0001.

4. Discussion

Biofabrication offers new approaches to tissue regeneration, screening and engineering alternatives to reduce animal experiments [35]. However, a paucity of *in vivo* studies evaluating safety and efficacy of 3D printed scaffolds for bone formation are currently reducing progress and limiting the clinical translation. In the current study, the skeletal functionality of HBMSCs-laden 3D bioprinted nanocomposite scaffolds has been investigated *in vitro, ex vivo* and *in vivo*. The results demonstrate significant improvements in mineralised tissue formation with addition of HBMSCs in 3DP, but not in mould casted bulk scaffolds.

The printing of bioinks laden with cells that can act as building blocks for the *in situ* generation of tissue-like structures represents a simple and efficacious approach to produce readily implantable constructs. However cell-laden bioinks should be printable [36, 37], generate constructs with elevated shape fidelity [38], and retain the potential to actively stimulate encapsulated cells post printing [7, 39, 40]. The nanocomposite matrix used as cell-delivering ink in this work was prepared from the inclusion of alginate and methylcellulose components in a nanoclay suspension (Laponite®). The smectite nanoclay, LAP, is able to intercalate even at low polymeric fractions between polymer chains of blended materials of interests [41, 42] to tailor cell detachment and cell-sheet formation [43], tune hydrogel shearing properties for delivery via injection [44] and modulate drug delivery and localisation [45].

In harnessing the properties of LAP, we have previously reported the use of the nanoclay as a ligand and filler for alginate and methylcellulose to produce a printable nanocomposite ink with the capability to encapsulate cells, aid cell growth and facilitate growth factor delivery *in vitro* [15]. The mechanical properties of printed nanocomposite ink were previously assessed and found to support the viability and proliferation of immortalised stem cells post-printing. The current studies detail the nanocomposite bioink, named 3-3-3, for the encapsulation and delivery of HBMSCs *in vivo* as a functional platform for the repair of large defects in non-load bearing sites.

Unselected HBMSCs loaded in the 3-3-3 bioink and printed, maintained their viability over 21 d of culture. Previous studies have shown that elevated cell density can significantly affect the rheological properties of a bioink and consequently printability [10] and viability of fabricated cell-laden constructs [46]. Cell density was observed to increase for up to 7 d of culture and to subsequently plateau at day 14. This observation has been reported previously in the literature [47, 48] with cells encapsulated at elevated densities demonstrating escape from the soft hydrogel network. Interestingly, in the current studies, the viability of the HBMSCs was unaffected by a decrease in cell density with cells present in the lattice structure, viable from day 14 to day 21 of culture.

Encapsulated cells were found to maintain their functional characteristics evidenced through ALP expression up to day 21 of culture *in vitro* when stimulated with basal and osteogenic media. This is notable, since enhanced ALP expression is rarely reported in HBMSCs-laden constructs at early time points (e.g. 3 d) [9] and, typically, is found extensively at later time points (between 1 and 2 weeks) [49, 50]. ALP is an early osteogenic marker [51] and its premature expression and decrease with time has been reported as a necessary step for bone nodule formation [52]. Indeed, Von Kossa staining confirmed an increase in

mineral deposition together with a decrease in ALP staining over 21 d, indicating a synergistic mechanism of skeletal tissue formation, driven initially by the printed HBMSCs and subsequently promoted by 3-3-3 mineralisation. The inherent and dose-dependent ability of LAP to initiate mineralisation in a saturated ionic solution has been reported before *in vitro* [53, 54]. Alginate/methylcellulose blend [55] was shown to be functionally active and to promote HBMSCs differentiation along the adipogenic lineage. The synergistic effects of matrix stiffness (alginate/methylcellulose) and clay-mediated bioactivity suggest that 3-3-3 scaffolds are able to support osteogenic differentiation of printed HBMSCs.

3D printed scaffolds implanted *ex vivo* in a CAM model proved the efficacy of the lattice structure to support angiogenesis with vessels penetrating the major pores. Indeed, vascular penetration has been reported to occur in scaffolds with interconnected porosity, that might stimulate angiogenesis, even in the absence of angiogenesis-inducing factors [56]. The addition of VEGF or HUVECs to these scaffolds further stimulated integration in the CAM and angiogenesis. Clotting of blood vessels has been previously reported linked to excessive functional stimuli provided to the host vasculature [57, 58] leading to a lack of patency of the neovascularisation and hence the leaking of blood. In particular, VEGF is known to stimulate vascular permeability [59], therefore localisation of excessive VEGF may have induced the leakage of the CAM membrane capillaries forming a clot as a consequence. VEGF and HUVECs stimuli could be further optimised to allow vascular induction reducing the leakage of blood vessels [60]. Combinations of HUVECs-seeded and VEGF-loaded scaffolds resulted in significant integration of the scaffolds and the CAM, with blood vessel penetration throughout the major pores with minimal clotting. The positive effects of VEGF on HUVECs in the presence of LAP have been previously reported [61]. Dawson *et al* [18] described the efficacious effects of VEGF localisation within LAP on angiogenesis both *in vitro* and *in vivo*. Recently, we have further investigated VEGF absorption and localisation in nanoclay-based 3D scaffolds [14, 48] within the CAM model, demonstrating the capacity of LAP to sustain the release of VEGF over time and to drive blood vessel formation and blood vessel penetration through 3D printed constructs. Similarly, 3-3-3 printed scaffolds adsorbed with VEGF, were found to support HUVECs functionality enhancing CAM integration and neovascularisation as evidenced by Chalkley score and histological analysis

Reproducing a clinical scenario and following a previously employed protocol [34], alginate controls and 3D printed 3-3-3 scaffolds containing adsorbed BMP-2 within the gel matrix were implanted in a mouse model to examine for ectopic bone formation. For the first time, we have here reported the

spontaneous mineralisation of acellular nanocomposite 3D printed constructs even in the absence of functional stimuli (e.g. BMP-2) *in vivo*. In a clinical scenario, for the repair of bone defects, BMP-2 is released from collagen sponges for a prolonged time [62] requiring a high dose of loading in the first instance [63]. This can lead to postoperative skeletal complications. Gibbs *et al* [34] demonstrated the clinical potential of BMP-2-loaded LAP gels confirming the functional retention and localisation ability of the nanoclay *in vivo* showing significant bone formation at physiological doses of BMP-2. Interestingly, in our study 3D printed scaffolds supplemented with BMP-2 were found to show elevated mineral density and distribution, losing their lattice structure to the mineral tissue, which was observed to fill the open pores of the scaffold, suggesting the localisation of the BMP-2 within the printed scaffold.

The fabrication of biomimetic three-dimensional constructs offers significant potential for clinical bone tissue regeneration. In the current study, we demonstrate the safety, efficacy and functionality of cell-laden (HBMSCs) 3-3-3 constructs in an *in vivo* subcutaneous implant model. Rapid growth of mineral density was found in all groups. Overall, 3D lattice constructs showed a higher bone volume and density compared to the casted controls as previously reported for porous scaffolds compared to bulk alternatives [64, 65]. 3D cell-laden printed implants were found to consistently produce the largest amount of mineralised tissue compared to all the other groups, confirming the synergistic effect of HBMSCs and nanoclay-based biomaterial. Recent studies have confirmed the beneficial results of HBMSCs inclusion in nanoclay, demonstrating enhanced bone deposition [66] and vascularisation [18] *in vivo*. However, cell-laden soft hydrogel constructs are not ideal matrices for the support of load-bearing portion of the skeletal tissue, which can be repaired using printed thermoplastic structures [67]. The current studies have examined bone formation in an ectopic model, a widely used industry standard model although in the absence of a load-bearing environment, the platform provides a model to assess efficacy with minimal injury addressing important principles around careful application of animal studies and replacement, refinement and reduction strategies around animal use. Critically, the current highly porous 3D printed lattice structure demonstrated an enhanced mineral deposition and reinforcement of the entire 3D scaffold. The mechanism at play is the focus of current work in our groups and the development and generation of reinforced complex 3D printed cellular nanocomposite scaffolds. The highly porous 3D printed lattice structure in the current studies, demonstrated an elevated mineral deposition with a consequent reinforcement of the entire 3D scaffold, possibly via a different mechanism from the mineralisation of casted controls. These appeared to be high density cluster networks,

comparable in density to the skeletal bones of the mouse, but with similar properties to the casted scaffolds. HBMSC-laden 3D bioprinted 3-3-3 constructs were found to follow a cluster mineralisation process, but showed a significant larger mineralised volume compared to the printed acellular controls. A greater difference in bone volume and average density of the mineralised tissue was observed when cell-laden lattice scaffolds were compared with acellular and cellular casted controls, suggesting a clear and significant advantage of the open porous cell-laden lattice structure. The mineral density was found to be well distributed within the scaffold with an elevated number of high-density clusters and a diffuse low-density matrix to encapsulate them. The bone formation mechanism can be related to the acellular clay-based 3D printed scaffolds with a high-density cluster-like arrangement due to the clay content. However, the lower density matrix surrounding the clusters was not found in the acellular printed controls, suggesting a novel remodelling and bioactive functional activity of the printed HBMSCs.

5. Conclusions

The potential to print stem cells, preserving cell viability, proliferation and functionality is a key unmet challenge for the biofabrication approach to regenerative medicine. Clay-based bioinks offer an attractive vehicle for printing HBMSCs in three-dimensional functional constructs due to their shear-thinning and inherent functional properties. In this study, we successfully demonstrated the biofabrication potential of a 3-3-3 bioink to produce viable and functional bone implants. In particular, printed HBMSCs-laden 3-3-3 demonstrated elevated viability and functionality *in vitro, ex vivo*, and critically, *in vivo*, indicating the translational potential of this nanocomposite bioink platform in combination with HBMSCs for the generation of large amounts of bone tissue. However, further studies are needed to elucidate the mechanism of mineralisation and bone formation (intramembranous, endochondral or a combination of both mechanisms). The lack of either *in vitro* or *in vivo* studies on the spontaneous mineralisation capacity of Laponite®-based bioinks makes this the first study to investigate such a process. Further confirmation will be needed to identify mineral deposition process and its origin in clay-based bioink. In summary, these results elucidate the promise of 3-3-3 printed scaffolds to produce mineral tissue *in vitro* and *in vivo* functionalised with either BMP-2 or HBMSCs for the formation of skeletal tissue.

Acknowledgments

Data availability

The raw/processed data required to reproduce these findings cannot be shared at this time due to technical or time limitations.

ORCID iDs

Michael Glinka ⓘ https://orcid.org/0000-0002-8278-5555
Tilman Ahlfeld ⓘ https://orcid.org/0000-0002-6350-3399
Anja Lode ⓘ https://orcid.org/0000-0001-7704-6435
Michael Gelinsky ⓘ https://orcid.org/0000-0001-9075-5121
Richard O C Oreffo ⓘ https://orcid.org/0000-0001-5995-6726

References

[1] Tang D, Tare R S, Yang L-Y, Williams D F, Ou K-L and Oreffo R O C 2016 Biofabrication of bone tissue: approaches, challenges and translation for bone regeneration. *Biomaterials* **83** 363–82

[2] Holmes A M, Charlton A, Derby B, Ewart L, Scott A and Shu W 2017 Rising to the challenge: applying biofabrication approaches for better drug and chemical product development *Biofabrication* **9** 1–20

[3] Sicari B M *et al* 2014 An acellular biologic scaffold promotes skeletal muscle formation in mice and humans with volumetric muscle loss *Sci. Transl. Med.* **6** 234ra58

[4] Jakus A E *et al* 2016 Hyperelastic "bone": a highly versatile, growth factor–free, osteoregenerative, scalable, and surgically friendly biomaterial *Sci. Transl. Med.* **8** 358ra127

[5] Dawson J I and Oreffo R O C 2008 Bridging the regeneration gap: stem cells, biomaterials and clinical translation in bone tissue engineering *Arch. Biochem. Biophys.* **473** 124–31

[6] Cidonio G, Glinka M, Dawson J I and Oreffo R O C 2019 The cell in the ink: improving biofabrication by printing stem cells for skeletal regenerative medicine *Biomaterials* **209** 10–24

[7] Murphy S V and Atala A 2014 3D bioprinting of tissues and organs *Nat. Biotechnol.* **32** 773–85

[8] Loozen L D, Wegman F, Öner F C, Dhert W J A and Alblas J 2013 Porous bioprinted constructs in BMP-2 non-viral gene therapy for bone tissue engineering *J. Mater. Chem.* B **1** 6619

[9] Fedorovich N E, De Wijn J R, Verbout A J, Alblas J and Dhert W J A 2008 Three-dimensional fiber deposition of cell-laden, viable, patterned constructs for bone tissue printing *Tissue Eng. Part* A **14** 127–33

[10] Hölzl K, Lin S, Tytgat L, Van Vlierberghe S, Gu L and Ovsianikov A 2016 Bioink properties before, during and after 3D bioprinting *Biofabrication* **8** 032002

[11] Lee M, Bae K, Guillon P, Chang J, Arlov Ø and Zenobi-Wong M 2018 Exploitation of cationic silica nanoparticles for bioprinting of large-scale constructs with high printing fidelity *ACS Appl. Mater. Interfaces* **10** 37820–8

[12] Zhu K *et al* 2017 Gold nanocomposite bioink for printing 3d cardiac constructs *Adv. Funct. Mater.* **27** 1–12

[13] Farahani R D, Dubé M and Therriault D 2016 Three-dimensional printing of multifunctional nanocomposites: manufacturing techniques and applications *Adv. Mater.* **28** 5794–821

[14] Cidonio G, Alcala-Orozco C R, Lim K S, Glinka M, Mutreja I, Y-h K, Dawson J I, Woodfield T B F and Oreffo R O C 2019 Osteogenic and angiogenic tissue formation in high fidelity nanocomposite Laponite-gelatin bioinks *Biofabrication* **11** 035027

[15] Ahlfeld T, Cidonio G, Kilian D, Duin S, Akkineni A R, Dawson J I, Yang S, Lode A, Oreffo R O C and Gelinsky M 2017 Development of a clay based bioink for 3D cell printing for skeletal application *Biofabrication* **9** 034103

[16] Ruzicka B and Zaccarelli E 2011 A fresh look at the Laponite phase diagram *Soft Matter* **7** 1268–86

[17] Carrow J K, Cross L M, Reese R W, Jaiswal M K, Gregory C A, Kaunas R, Singh I and Gaharwar A K 2018 Widespread changes in transcriptome profile of human mesenchymal stem cells induced by two-dimensional nanosilicates *Proc. Natl. Acad. Sci.* **115** E3905–13

[18] Dawson J I, Kanczler J M, Yang X B, Attard G S and Oreffo R O C 2011 Clay gels for the delivery of regenerative microenvironments *Adv. Mater.* **23** 3304–8

[19] Shi P, Kim Y H, Mousa M, Sanchez R R, Oreffo R O C and Dawson J I 2018 Self-assembling nanoclay diffusion gels for bioactive osteogenic microenvironments *Adv. Healthcare Mater.* **7** 1800331

[20] Zhai X, Ma Y, Hou C, Gao F, Zhang Y, Ruan C, Pan H, Lu W W and Liu W 2017 3D-printed high strength bioactive supramolecular polymer/clay nanocomposite hydrogel scaffold for bone regeneration. *ACS Biomater Sci. Eng.* **3** 1109–18

[21] Rodriguez M J, Dixon T A, Cohen E, Huang W, Omenetto F G and Kaplan D L 2018 3D freeform printing of silk fibroin *Acta Biomater.* **71** 379–87

[22] Peak C W, Stein J, Gold K A and Gaharwar A K 2018 Nanoengineered colloidal inks for 3d bioprinting *Langmuir* **34** 917–25

[23] Xavier J R, Thakur T, Desai P, Jaiswal M K, Sears N, Cosgriff-Hernandez E, Kaunas R and Gaharwar A K 2015 Bioactive nanoengineered hydrogels for bone tissue engineering: a growth-factor-free approach *ACS Nano* **9** 3109–18

[24] Chimene D, Peak C W, Gentry J L, Carrow J K, Cross L M, Mondragon E, Cardoso G B, Kaunas R and Gaharwar A K 2018 Nanoengineered ionic–covalent entanglement (NICE) bioinks for 3d bioprinting *ACS Appl. Mater. Interfaces* **10** 9957–68

[25] Dávila J L and D'Ávila M A 2019 Rheological evaluation of Laponite/alginate inks for 3D extrusion-based printing *Int. J. Adv. Manuf. Technol.* **101** 675–86

[26] Hong S, Sycks D, Chan H F, Lin S, Lopez G P, Guilak F, Leong K W and Zhao X 2015 3D printing: 3d printing of highly stretchable and tough hydrogels into complex, cellularized structures *Adv. Mater.* **27** 4034

[27] Zhai X, Ruan C, Ma Y, Cheng D, Wu M, Liu W, Zhao X, Pan H and Lu W W 2018 3D-bioprinted osteoblast-laden nanocomposite hydrogel constructs with induced microenvironments promote cell viability, differentiation, and osteogenesis both *in vitro* and *in vivo Adv. Sci.* **5** 1700550

[28] Kanczler J, Tare R S, Stumpf P, Noble T J, Black C and Oreffo R O C 2019 Isolation, differentiation, and characterization of human bone marrow stem cells *in vitro* and *in vivo Bone Research Protocols* (New York: Humana Press) pp 53–70

[29] Jaffe E A, Nachman R L, Becker C G and Minick C R 1973 Culture of human endothelial cells derived from umbilical veins. Identification by morphologic and immunologic criteria *J. Clin. Invest.* **52** 2745–56

[30] Inglis S, Kanczler J M and Oreffo R O C 2018 3D human bone marrow stromal and endothelial cell spheres promote bone healing in an osteogenic niche *FASEB J.* **33** 3279–90

[31] Vaezi M, Black C, Gibbs D M R, Oreffo R O C, Brady M, Moshrefi-Torbati M and Yang S 2016 Characterization of

New PEEK/HA composites with 3D HA network fabricated by extrusion freeforming *Molecules* **21** 1–21

[32] Czekanska E M, Geng J, Glinka M, White K, Kanczler J, Evans N D, Oreffo R O C and Bradley M 2018 Combinatorial delivery of bioactive molecules by a nanoparticle-decorated and functionalized biodegradable scaffold *J. Mater. Chem.* B **6** 4437–45

[33] Kawamoto T and Shimizu M 2000 A method for preparing 2- to 50-micron-thick fresh-frozen sections of large samples and undecalcified hard tissues *Histochem. Cell Biol.* **113** 331–9

[34] Gibbs D M R, Black C R M, Hulsart-Billstrom G, Shi P, Scarpa E, Oreffo R O C and Dawson J I 2016 Bone induction at physiological doses of BMP through localization by clay nanoparticle gels *Biomaterials* **99** 16–23

[35] Otto I A, Breugem C C, Malda J and Bredenoord A L 2016 Ethical considerations in the translation of regenerative biofabrication technologies into clinic and society *Biofabrication* **8** 042001

[36] Paxton N, Smolan W, Böck T, Melchels F, Groll J and Jungst T 2017 Proposal to assess printability of bioinks for extrusion-based bioprinting and evaluation of rheological properties governing bioprintability *Biofabrication* **9** 044107

[37] He Y, Yang F, Zhao H, Gao Q, Xia B and Fu J 2016 Research on the printability of hydrogels in 3D bioprinting *Sci. Rep.* **6** 29977

[38] Ribeiro A, Blokzijl M M, Levato R, Visser C W, Castilho M, Hennink W E, Vermonden T and Malda J 2017 Assessing bioink shape fidelity to aid material development in 3D bioprinting *Biofabrication* **10** 014102

[39] Zhu W, Ma X, Gou M, Mei D, Zhang K and Chen S 2016 3D printing of functional biomaterials for tissue engineering *Curr. Opin. Biotechnol.* **40** 103–12

[40] Williams D, Thayer P, Martinez H, Gatenholm E and Khademhosseini A 2018 A perspective on the physical, mechanical and biological specifications of bioinks and the development of functional tissues in 3D bioprinting *Bioprinting* **9** 19–36

[41] Okada A and Usuki A 2006 Twenty years of polymer-clay nanocomposites *Macromol. Mater. Eng.* **291** 1449–76

[42] Ruiz-Hitzky E, Aranda P, Darder M and Rytwo G 2010 Hybrid materials based on clays for environmental and biomedical applications *J. Mater. Chem.* **20** 9306–21

[43] Haraguchi K 2012 Development of soft nanocomposite materials and their applications in cell culture and tissue engineering *J. Stem Cells Regen. Med.* **14:8** 2–11

[44] Gaharwar A K, Avery R K, Assmann A, Paul A, McKinley G H, Khademhosseini A and Olsen B D 2014 Shear-thinning nanocomposite hydrogels for the treatment of hemorrhage *ACS Nano* **8** 9833–42

[45] Viseras C, Aguzzi C, Cerezo P and Bedmar M C 2008 Biopolymer–clay nanocomposites for controlled drug delivery *Mater. Sci. Technol.* **24** 1020–6

[46] Billiet T, Gevaert E, De Schryver T, Cornelissen M and Dubruel P 2014 The 3D printing of gelatin methacrylamide cell-laden tissue-engineered constructs with high cell viability *Biomaterials* **35** 49–62

[47] Cavo M, Caria M, Pulsoni I, Beltrame F, Fato M and Scaglione S 2018 A new cell-laden 3D Alginate-Matrigel hydrogel resembles human breast cancer cell malignant morphology, spread and invasion capability observed "*in vivo*" *Sci. Rep.* **8** 1–12

[48] Cidonio G, Cooke M, Glinka M, Dawson J I, Grover L and Oreffo R O C 2019 Printing bone in a gel: using nanocomposite bioink to print functionalised bone scaffolds *Mater. Today Bio* **4** 100028

[49] Fedorovich N E, Kuipers E, Gawlitta D, Dhert W J A and Alblas J 2011 Scaffold porosity and oxygenation of printed hydrogel constructs affect functionality of embedded osteogenic progenitors *Tissue Eng. Part* A **17** 2473–86

[50] Lim K S *et al* 2018 Bio-resin for high resolution lithography-based biofabrication of complex cell-laden constructs *Biofabrication* **10** 034101

[51] Jaiswal N, Haynesworth S E, Caplan A I and Bruder S P 1997 Osteogenic differentiation of purified, culture-expanded human mesenchymal stem cells in vitro *J. Cell. Biochem.* **64** 295–312

[52] Malaval L, Modrowski D, Gupta A K and Aubin J E 1994 Cellular expression of bone-related proteins during in vitro osteogenesis in rat bone marrow stromal cell cultures *J. Cell. Physiol.* **158** 555–72

[53] Gaharwar A K, Mukundan S, Karaca E, Dolatshahi-Pirouz A, Patel A, Rangarajan K, Mihaila S M, Iviglia G, Zhang H and Khademhosseini A 2014 Nanoclay-enriched poly(ε-caprolactone) electrospun scaffolds for osteogenic differentiation of human mesenchymal stem cells *Tissue Eng. Part* A **20** 2088–101

[54] Wang C, Wang S, Li K, Ju Y, Li J, Zhang Y, Li J, Liu X, Shi X and Zhao Q 2014 Preparation of laponite bioceramics for potential bone tissue engineering applications *PLoS ONE* **9** 1–12

[55] Schütz K, Placht A-M, Paul B, Brüggemeier B, Gelinsky M and Lode A 2015 Three-dimensional plotting of a cell-laden alginate/ methylcellulose blend: towards biofabrication of tissue engineering constructs with clinically relevant dimensions *J. Tissue Eng. Regen. Med.* **2** 408–17

[56] Xiao X, Wang W, Liu D, Zhang H, Gao P, Geng L, Yuan Y, Lu J and Wang Z 2015 The promotion of angiogenesis induced by three-dimensional porous beta-tricalcium phosphate scaffold with different interconnection sizes via activation of PI3K/Akt pathways *Sci. Rep.* **5** 9409

[57] Wilting J, Christ B, Bokeloh M and Weich H A 1993 In vivo effects of vascular endothelial growth factor on the chicken chorioallantoic membrane *Cell Tissue Res.* **274** 163–72

[58] Strassburg S, Nienhueser H, Björn Stark G, Finkenzeller G and Torio-Padron N 2016 Co-culture of adipose-derived stem cells and endothelial cells in fibrin induces angiogenesis and vasculogenesis in a chorioallantoic membrane model *J. Tissue Eng. Regen. Med.* **10** 496–506

[59] Bates D O 2010 Vascular endothelial growth factors and vascular permeability *Cardiovasc. Res.* **87** 262–71

[60] Bai Y, Bai L, Zhou J, Chen H and Zhang L 2018 Sequential delivery of VEGF, FGF-2 and PDGF from the polymeric system enhance HUVECs angiogenesis in vitro and CAM angiogenesis *Cell. Immunol.* **323** 19–32

[61] Armesilla A L, Lorenzo E, Gómez Del Arco P, Martínez-Martínez S, Alfranca A and Redondo J M 2015 Vascular endothelial growth factor activates nuclear factor of activated T cells in human endothelial cells: a role for tissue factor gene expression *Mol. Cell. Biol.* **19** 2032–43

[62] Uludag H, D'Augusta D, Palmer R, Timony G and Wozney J 1999 Characterization of rhBMP-2 pharmacokinetics implanted with biomaterial carriers in the rat ectopic model *J. Biomed. Mater. Res.* **46** 193–202

[63] Shields L B E, Raque G H, Glassman S D, Campbell M, Vitaz T, Harpring J and Shields C B 2006 Adverse effects associated with high-dose recombinant human bone morphogenetic protein-2 use in anterior cervical spine fusion *Spine* **31** 542–7

[64] Gonzalez-Fernandez T *et al* 2019 Pore-forming bioinks to enable spatio-temporally defined gene delivery in bioprinted tissues *J. Control. Release* **301** 13–27

[65] Daly A C, Pitacco P, Nulty J, Cunniffe G M and Kelly D J 2018 3D printed microchannel networks to direct vascularisation during endochondral bone repair *Biomaterials* **162** 34–46

[66] Li T, Liu Z L, Xiao M, Yang Z Z, Peng M Z, Li C D, Zhou X J and Wang J W 2018 Impact of bone marrow mesenchymal stem cell immunomodulation on the osteogenic effects of laponite *Stem Cell Res. Ther.* **9** 100

[67] Schuurman W, Khristov V, Pot M W, van Weeren P R, Dhert W J A and Malda J 2011 Bioprinting of hybrid tissue constructs with tailorable mechanical properties *Biofabrication* **3** 021001